ACS OMEGA

http://pubs.acs.org/journal/acsodf

Article

Tween-20-Modified $BiVO_4$ Nanorods for CT Imaging-Guided Radiotherapy of Tumor

Bo Peng, Yifan Hao, Chao Si, Bo Wang, Chengfeng Luo, Menghao Chen, Cheng Luo, Baijuan Gong, and Zhimin Li*

Cite This: *ACS Omega* 2023, 8, 4736−4746

Read Online

ACCESS | Metrics & More | Article Recommendations | Supporting Information

ABSTRACT: Oral cancer is the most common malignant tumor in the oral and maxillofacial region, which seriously threatens the health of patients. At present, radiotherapy is one of the commonly used methods for oral cancer treatment. However, the resistance of cancerous tissues to ionizing radiation, as well as the side effects of X-rays on healthy tissues, still limit the application of radiotherapy. Therefore, how to effectively solve the above problems is still a challenge at present. Generally speaking, elements with high atomic numbers, such as bismuth, tungsten, and iodine, have a high X-ray attenuation capacity. Using nanomaterials containing these elements as radiosensitizers can greatly improve the radiotherapy effect. At the same time, the modification of nanomaterials based on the above elements with the biocompatible polymer can effectively reduce the side effects of radiosensitizers, providing a new method for the realization of efficient and safe radiotherapy for oral cancer. In this work, we prepared Tween-20-modified $BiVO_4$ nanorods (Tw20-$BiVO_4$ NRs) and further used them in the radiotherapy of human tongue squamous cell carcinoma. Tw20-$BiVO_4$ NRs are promising radiosensitizers, which can generate a large number of free radicals under X-rays, leading to the damage of cancer cells and thus playing a role in tumor therapy. In cell experiments, radiotherapy sensitization of Tw20-$BiVO_4$ NRs significantly enhanced the production of free radicals in oral cancer cells, aggravated the destruction of chromosomes, and improved the therapeutic effect of radiotherapy. In animal experiments, the strong X-ray absorption ability of Tw20-$BiVO_4$ NRs makes them effective contrast agents in computed tomography (CT) imaging. After the tumors are located by CT imaging, it helps to apply precise radiotherapy; the growth of subcutaneous tumors in nude mice was significantly inhibited, confirming the remarkable effect of CT imaging-guided radiotherapy.

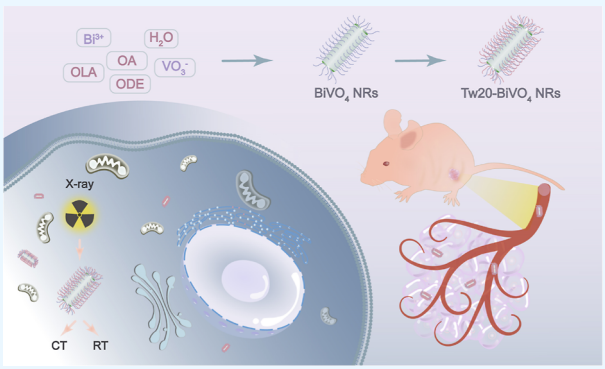

INTRODUCTION

Oral cancer is a malignant tumor occurring in the oral and maxillofacial region.[1] In recent years, the incidence of oral cancer has been increasing year by year, seriously threatening the health of patients.[2,3] Because of the particularity of the location, oral cancer is not easy to be found; thus, it is difficult to achieve early detection and early treatment.[4,5] In addition, oral cancer easily metastasizes to cervical lymph nodes, and the cure rate and survival rate are very low.[6] In the treatment of oral cancer, radiotherapy is a common method.[7,8] Radiotherapy is a treatment based on ionizing radiation, which can inhibit cell proliferation by damaging the DNA of oral cancer cells and then treat oral cancer, showing certain effects.[9] However, the efficacy of radiotherapy is generally limited by insufficient radiation energy deposition, radioresistance on tumor tissues, and the side effects on normal tissues.[10,11] Therefore, how to effectively solve the current problems in clinical radiotherapy is still a challenge at present.

In the process of radiotherapy, reactive oxygen species (ROS) have proven to play an important role as mediators of DNA damage to effectively destroy the proliferation ability of cancer cells and inhibit tumor growth.[12,13] Therefore, enhancing the production of ROS is an effective method to improve the efficacy of radiotherapy, which also leads to the demand for efficient radiosensitizers. Radiosensitization refers to the process of using some drugs or physical methods to improve the sensitivity of cancer cells to radiation to enhance the killing effect of radiation on cancer cells and improve the control rate and cure rate of malignant tumors. Radiosensitizers are chemical or pharmaceutical agents that can sensitize radiotherapy; when used under X-rays, they can increase the content of ROS in cancer cells, damage DNA, and change the sensitivity of tumor cells to radiation, thus

Received: October 18, 2022
Accepted: January 16, 2023
Published: January 25, 2023

ACS Publications

© 2023 The Authors. Published by American Chemical Society

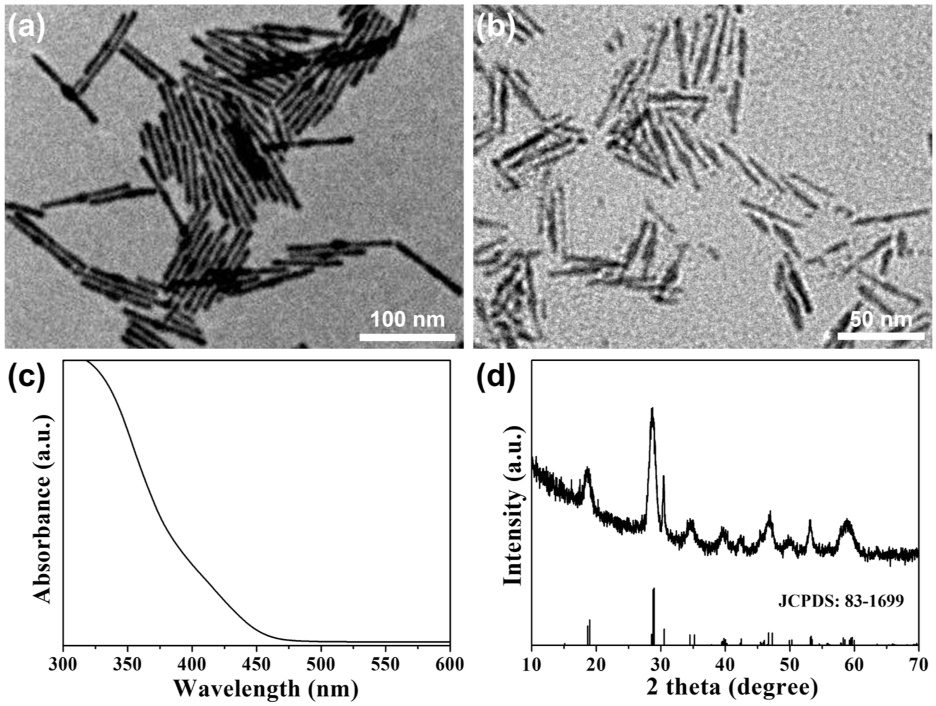

Figure 1. (a) Transmission electron microscopy (TEM) image of $BiVO_4$ NRs. (b) TEM image of Tw20-$BiVO_4$ NRs. (c) Absorption spectrum of Tw20-$BiVO_4$ NRs. (d) XRD pattern of Tw20-$BiVO_4$ NRs.

increasing the killing effect on cancer cells.[9,14−17] The research on new radiosensitizers has become a hot spot in the current research, which can improve the lethality of the tumor by producing a large number of ROS in the course of radiotherapy.

With the development of nanotechnology in the past decade, radiosensitizers based on nanomaterials stand out from other kinds of radiosensitizers and have received extensive attention. Nanomaterials containing high atomic number elements are attracting considerable critical attention, which can absorb X-rays not only to act as radiosensitizers to deposit radiation energy and secondary electrons within DNA but also have the ability to increase ROS generation to make cancer cells more sensitive to radiation.[15,18−20] Specifically, the relationship between the X-ray absorption coefficient (μ) and the atomic number (Z) can be expressed as $\mu = \rho Z^4/(AE^3)$, where A is the atomic mass and E is the X-ray energy, indicating that nanomaterials that possess higher density (ρ) or atomic number (Z) are inclined to have stronger X-ray attenuation ability and better X-ray absorption. The strong relationship ($\mu \sim Z^4$) between the X-ray absorption coefficient and atomic number is of great significance for developing radiosensitizers.[21,22] Until now, many radiosensitizers containing high-Z elements have been explored to improve the radiotherapeutic efficacy, including Au,[23] W,[24] Bi,[25−28] I,[29] Gd,[30] etc.[15,31] Among these radiosensitizers, Bi-based nanomaterials attract particular interest because of their highest atomic number element (Z = 83) among all nonradiative elements, K-edge value of 90.5 keV, and excellent X-ray attenuation properties (5.74 $cm^2\ g^{-1}$ at 100 keV), which are strongly favorable for application in radiosensitizers.[18,32−34] Moreover, Bi is very stable at room temperature and less toxic, which could be applied to various medical applications.[32,35−38] As a result, the development of biocompatible and efficient Bi-based nanomaterials as radiosensitizers is of great significance to improve the efficacy of radiotherapy-related treatments.

At the same time, the strong relationship ($\mu \sim Z^4$) between the X-ray absorption coefficient and the atomic number is also of great significance for X-ray computed tomography (CT) imaging.[21,39] CT is one of the most powerful and widely used imaging modalities in the diagnosis of a wide variety of diseases.[40,41] However, because of the similar CT density of most soft tissues, CT has absolute inferiority in the accurate diagnosis of soft tissue lesions, including tumors. Therefore, it is extremely necessary to enhance the contrast between the tumor and peritumoral tissues with CT contrast agents and further achieve the precise detection of the tumor.[42,43] Using nanomaterials containing high-Z elements as contrast agents for CT imaging can exhibit more advantages in terms of intrinsic contrast, lower dose requirement, and lower radiation exposure to patients than low-Z elements materials.[37,42,44] As mentioned above, Bi, with a high atomic number and a high K-edge energy which falls within the diagnostic energy range employed by many clinical CT imaging scanners, has shown huge promise as a contrast agent for CT imaging applications. Therefore, Bi-containing nanomaterials are helpful to realize CT imaging-guided tumor radiotherapy.[45−48] Under the enhanced permeability and retention effect, nanomaterials are enriched at the tumor sites, and CT imaging can accurately identify the location of the tumors, guiding the application of precise X-ray irradiation. At the same time, it is very beneficial to reduce the side effects of radiotherapy.[40,49−52] Furthermore, the design and synthesis of new Bi-containing nanomaterials are consistent with the notion of multifunctional nanotheranostics for multimodal imaging-guided synergistic therapy, which has allowed for maximizing the effectiveness of theranostics while minimizing potential adverse effects under the condition of the precise control of X-ray dose.[31]

https://doi.org/10.1021/acsomega.2c06714
ACS Omega 2023, 8, 4736−4746

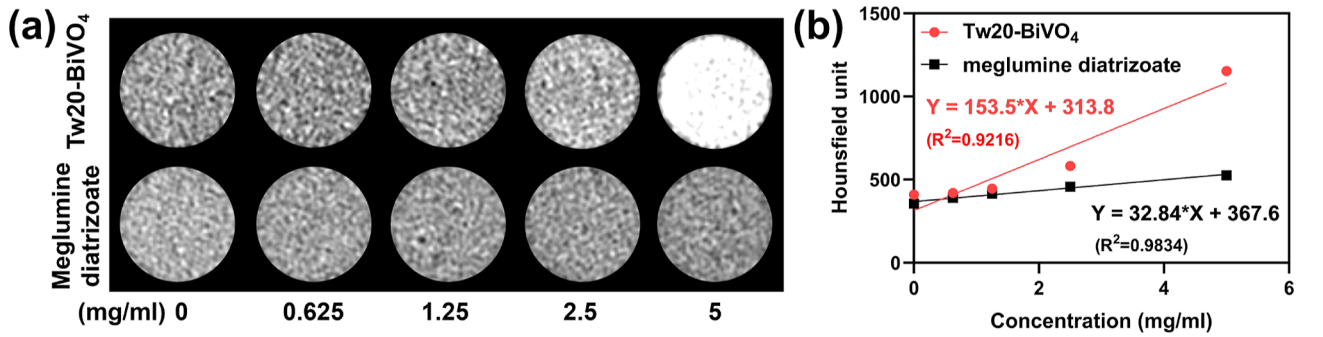

Figure 2. (a) CT imaging of Tw20-$BiVO_4$ NRs and diatrizoate meglumine at different concentrations. (b) HU values of Tw20-$BiVO_4$ NRs and diatrizoate meglumine obtained by fitting CT imaging data from linear regression.

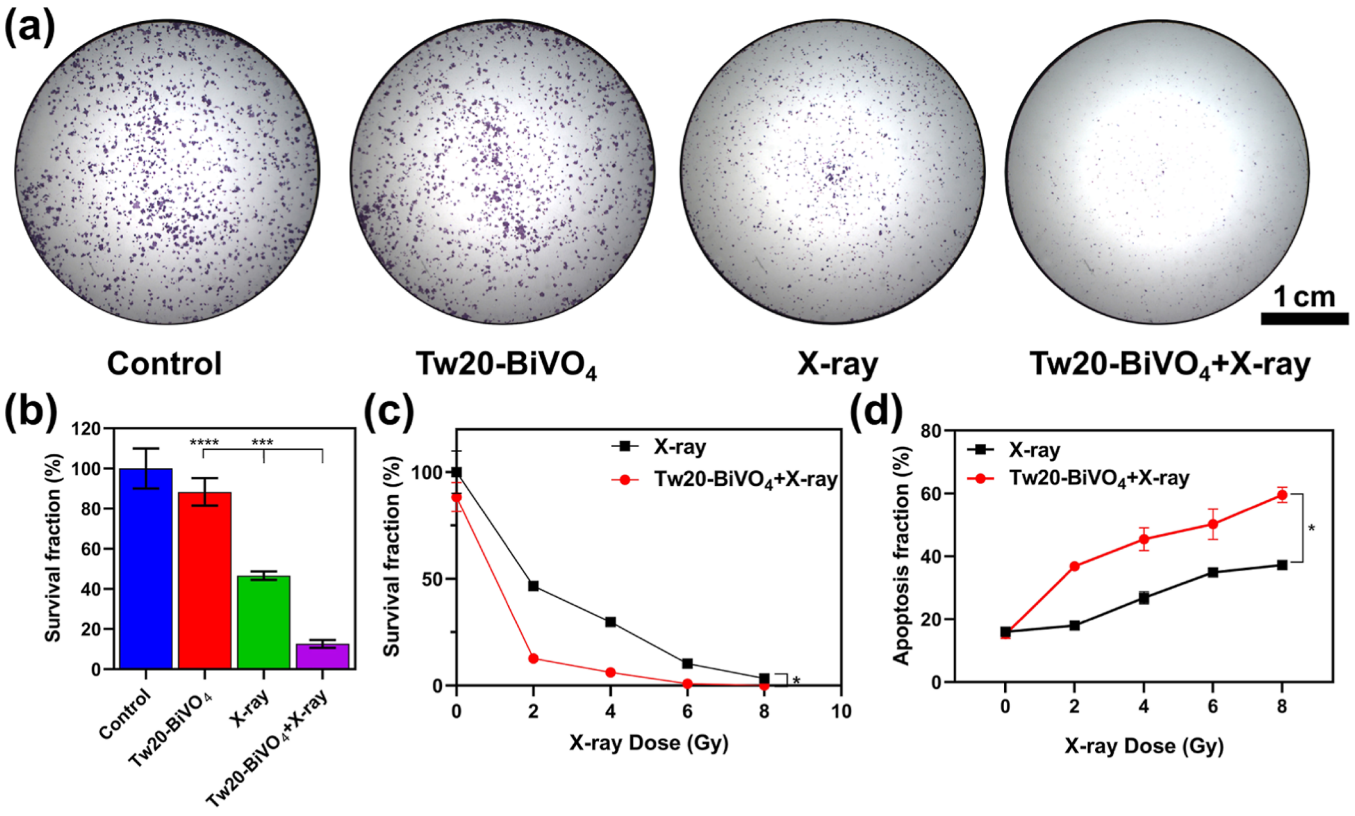

Figure 3. (a) Clonogenic assay of CAL27 cells under different treatments (X-ray dose: 2 Gy). (b) Corresponding survival fraction of colony formation assay under different treatments using ordinary one-way ANOVA (X-ray dose: 2 Gy). (c) Survival fraction of CAL27 cells under different treatments and different X-ray doses using the paired *T*-test. (d) Proportion of apoptosis of CAL27 cells under different treatments and different X-ray doses conducted by flow cytometry using the paired *T*-test. $^*P < 0.05$, $^{***}P < 0.001$, and $^{****}P < 0.0001$.

In this work, we succeeded in designing and preparing Tween-20-modified $BiVO_4$ nanorods (Tw20-$BiVO_4$ NRs) for CT imaging-guided tumor radiotherapy, which not only identified the location of tumors and guided precise radiotherapy but also enhanced radiotherapy sensitivity and reduced the side effects of radiotherapy. In cell experiments, radiotherapy sensitization of Tw20-$BiVO_4$ NRs significantly enhanced the production of free radicals in oral cancer cells, aggravated the destruction of chromosomes, and improved the therapeutic effect of radiotherapy. In animal experiments, the tumors were precisely located by CT imaging, and under the action of X-rays the growth of subcutaneous tumors in nude mice was significantly inhibited, confirming the remarkable effect of CT imaging-guided radiotherapy. We firmly believe that Tw20-$BiVO_4$ NRs will have great application prospects in the field of nanotheranostics.

RESULTS AND DISCUSSION

Structure and Function of Tw20-$BiVO_4$ NRs. First, we synthesized $BiVO_4$ NRs in the oil phase using oleylamine (OLA) and oleic acid (OA) as ligands, which are shown in Figure 1a (we can see that they have a uniform and regular one-dimensional morphology). Then, we modified their surface with the highly biocompatible polymer Tween-20 to transfer them from the oil phase to the water phase, which is shown in Figure 1b. They still maintained one-dimensional morphology, so the modification of the polymer Tween-20 does not change their morphology. Figure 1c shows the absorption spectrum of the Tw20-$BiVO_4$ NRs. There was an

https://doi.org/10.1021/acsomega.2c06714
ACS Omega 2023, 8, 4736−4746

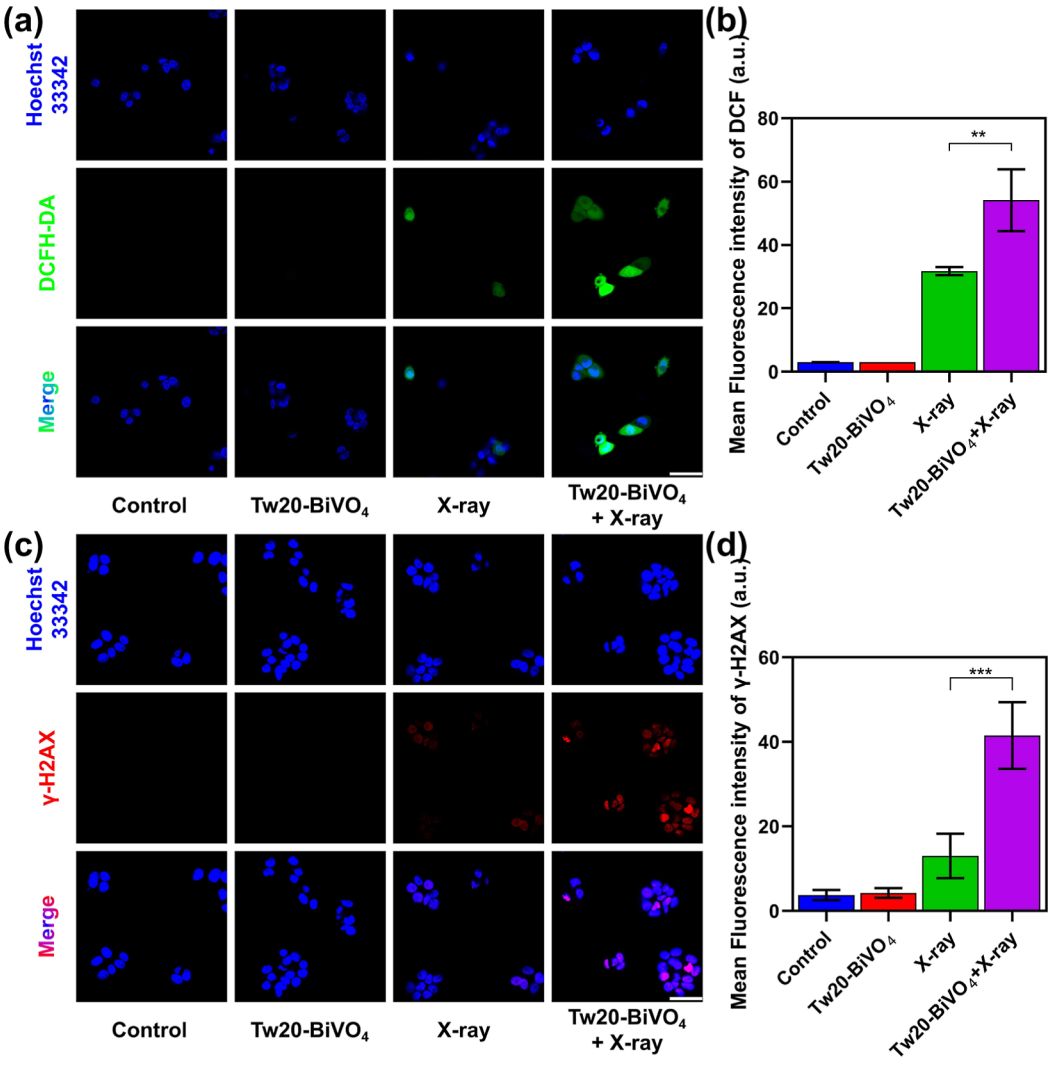

Figure 4. (a) ROS staining in CAL27 cells under different treatments; the scale bar is 50 μm. (b) Corresponding fluorescence intensities obtained by ordinary one-way ANOVA. (c) γ-H2AX staining in CAL27 cells under different treatments, the scale bar is 50 μm. (d) Corresponding fluorescence intensities obtained by ordinary one-way ANOVA. $^{**}P < 0.01$ and $^{***}P < 0.001$.

absorption edge at about 475 nm and no obvious absorption peak, which corresponds to $BiVO_4$. Figure 1d shows the X-ray diffraction (XRD) pattern of the $BiVO_4$ NRs, which corresponds well to the standard spectrum of monoclinic $BiVO_4$ (JCPDS: 83-1699). The narrow and sharp peaks demonstrate the good crystallinity of the Tw20-$BiVO_4$ NRs.

The as-prepared Tw20-$BiVO_4$ NRs have a high Bi content. Because of the high X-ray absorption coefficient of Bi, Tw20-$BiVO_4$ NRs can be used as a CT imaging contrast agent. With increasing concentration of Tw20-$BiVO_4$ NRs solution, the CT signal gradually increased and was higher than the clinically used CT contrast agent diatrizoate meglumine with the same concentrations (Figure 2a). The Hounsfield unit (HU) values were obtained by fitting CT imaging data. The HU value of Tw20-$BiVO_4$ NRs was calculated to be 153.5 HU mL mg^{-1}, while that of diatrizoate meglumine was 32.84 HU mL mg^{-1} (Figure 2b). Tw20-$BiVO_4$ NRs have good CT imaging ability in vitro.

Radiosensitization in Cells. In the cell experiment, in vitro cytotoxicity was first tested to evaluate whether Tw20-$BiVO_4$ NRs meet the biosafety requirements for imaging and therapy application. After incubation with Tw20-$BiVO_4$ NRs for 24 h, the relative viability of CAL27 cells was measured by flow cytometry. As shown in Figure S1, Tw20-$BiVO_4$ NRs exhibited no significant toxicity to CAL27 cells even when the concentration was as high as 200 μg/mL. The results of multiple flow cytometry data showed the same results, suggesting that Tw20-$BiVO_4$ NRs have good biocompatibility for biomedical applications (Figure S2).

To prove radiosensitization, the proliferative inhibitory ability of Tw20-$BiVO_4$ NRs on tumor cells was investigated by clonogenic assay to evaluate the radiosensitizing effect of Tw20-$BiVO_4$ NRs in vitro. The results of the experiment showed that the Tw20-$BiVO_4$ NRs alone group had little effect on the cell proliferation ability, and the X-ray alone group had shown the effect of radiotherapy (Figure 3a). After being irradiated with only 2 Gy X-rays, the survival fraction of CAL27 cells was 46.66%. However, the cell survival fraction was only 12.62% under the synergistic effect of Tw20-$BiVO_4$ NRs and X-rays (Figure 3b). With the increase of X-ray irradiation intensity, the survival fraction of CAL27 cells decreased gradually, which reflects the enhanced radiotherapy efficacy (Figure 3c).

https://doi.org/10.1021/acsomega.2c06714
ACS Omega 2023, 8, 4736−4746

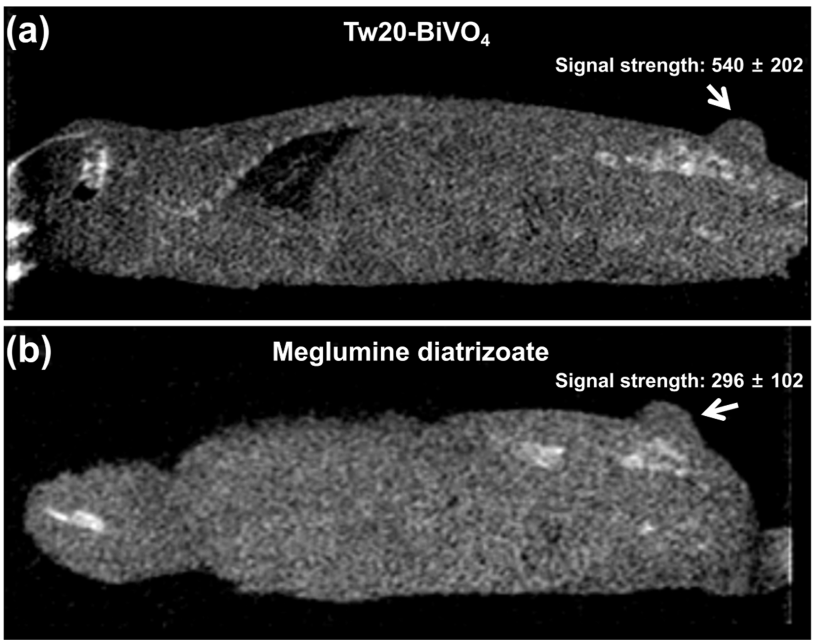

Figure 5. (a) In vivo CT image of the mouse intravenously injected with Tw20-$BiVO_4$ NRs. (b) In vivo CT image of the mouse intravenously injected with meglumine diatrizoate.

On the basis of the clonogenic assay experiment, we compared the effects of radiotherapy in the presence or absence of Tw20-$BiVO_4$ NRs. As shown in Figure S3, under the same radiation doses, Tw20-$BiVO_4$ NRs can significantly increase the proportion of apoptosis. In order to reflect the radiosensitization effect more directly, the results of flow cytometry were further drawn into a line graph, which indicated that the differences were statistically significant (Figure 3d). The statistical analysis results showed that the presence or not of Tw20-$BiVO_4$ NRs had a very significant impact on the survival fraction and apoptosis fraction of CAL27 cells. Both the clonogenic assay and flow cytometry certify strong inhibition to cell proliferation of Tw20-$BiVO_4$ NRs, and the radiosensitization effect of Tw20-$BiVO_4$ NRs was excellent. Even under lower X-ray radiation doses, Tw20-$BiVO_4$ NRs can also achieve promising therapeutic effects, which is helpful to reduce the side effects that are usually caused by excessive X-ray radiation.

Recent research has suggested that excessive ROS accumulation induced by ionizing radiation played an important role in DNA fragmentation and subsequent cell death.[53] In relevant experimental studies, a 2′,7′-dichlorodihydrofluorescein diacetate (DCFH-DA) fluorescent probe was employed to detect intracellular ROS levels of CAL27 cells after different treatments.[54] As shown in Figure 4a, cell nuclei were labeled with blue fluorescence, and ROS were labeled with green fluorescence. Almost no green fluorescence was observed in the control group and the Tw20-$BiVO_4$ NRs group, and a small amount of green fluorescence appeared in the X-ray group, indicating that X-ray alone could lead to the generation of ROS. Under the joint action of Tw20-$BiVO_4$ NRs and X-rays, a large number of intracellular ROS were generated. The relative fluorescence intensity measured by ImageJ software directly reflected the differences in ROS levels in each group (Figure 4b). Furthermore, the fluorescence signal of DCFH-DA was quantitatively analyzed by flow cytometry. As shown in Figure S4, the ROS levels in the cells showed significant differences under four different experimental treatments. The intensity of green fluorescence was 10.5 times higher in the X-ray-alone group than in the control group, while for the Tw20-$BiVO_4$ NRs + X-ray group, the intensity of green fluorescence was 17.9 times higher than that of the control group.

Since high-radiation energy deposition and enhanced oxidative stress may facilitate the damage of DNA, γ-H2AX staining was performed to analyze the damage to DNA double-strands in cell nuclei.[12] Similar to the ROS assay, no visible fluorescence was found in the cells without X-ray treatment. The apparent fluorescence could be seen in the cells in the treatment groups of X-ray and Tw20-$BiVO_4$ NRs + X-ray. In line with the expectations, the Tw20-$BiVO_4$ NRs + X-ray treatment induced the highest fluorescence intensity, which means severe DNA damage (Figure 4c). Then, the relative fluorescence intensity was analyzed by the ImageJ software. Figure 4d provides an overview of the fluorescence intensity among the different groups, and the differences between X-ray treatment and Tw20-$BiVO_4$ NRs + X-ray treatment were statistically significant. Both DCFH-DA and γ-H2AX assays demonstrated the favorable radiosensitization activity of Tw20-$BiVO_4$ NRs, which could induce intracellular massive ROS under X-ray radiation to damage the double-stranded DNA in cell nuclei.

CT Imaging-Guided Radiotherapy In Vivo. Motivated by the favorable outcomes in vitro, we then investigated the CT imaging-guided radiotherapy performance of Tw20-$BiVO_4$ NRs in vivo. Balb/c nude mice with subcutaneous tumors in the buttocks were selected as tumor models, and the drug administration method used in the experiment was tail vein injection. Tumors in mice injected with Tw20-$BiVO_4$ NRs showed stronger CT signals than those injected with the contrast agent meglumine diatrizoate (Figure 5a,b). Tw20-$BiVO_4$ NRs showed better CT imaging results than the commonly used contrast media in clinical practice.

https://doi.org/10.1021/acsomega.2c06714
ACS Omega 2023, 8, 4736−4746

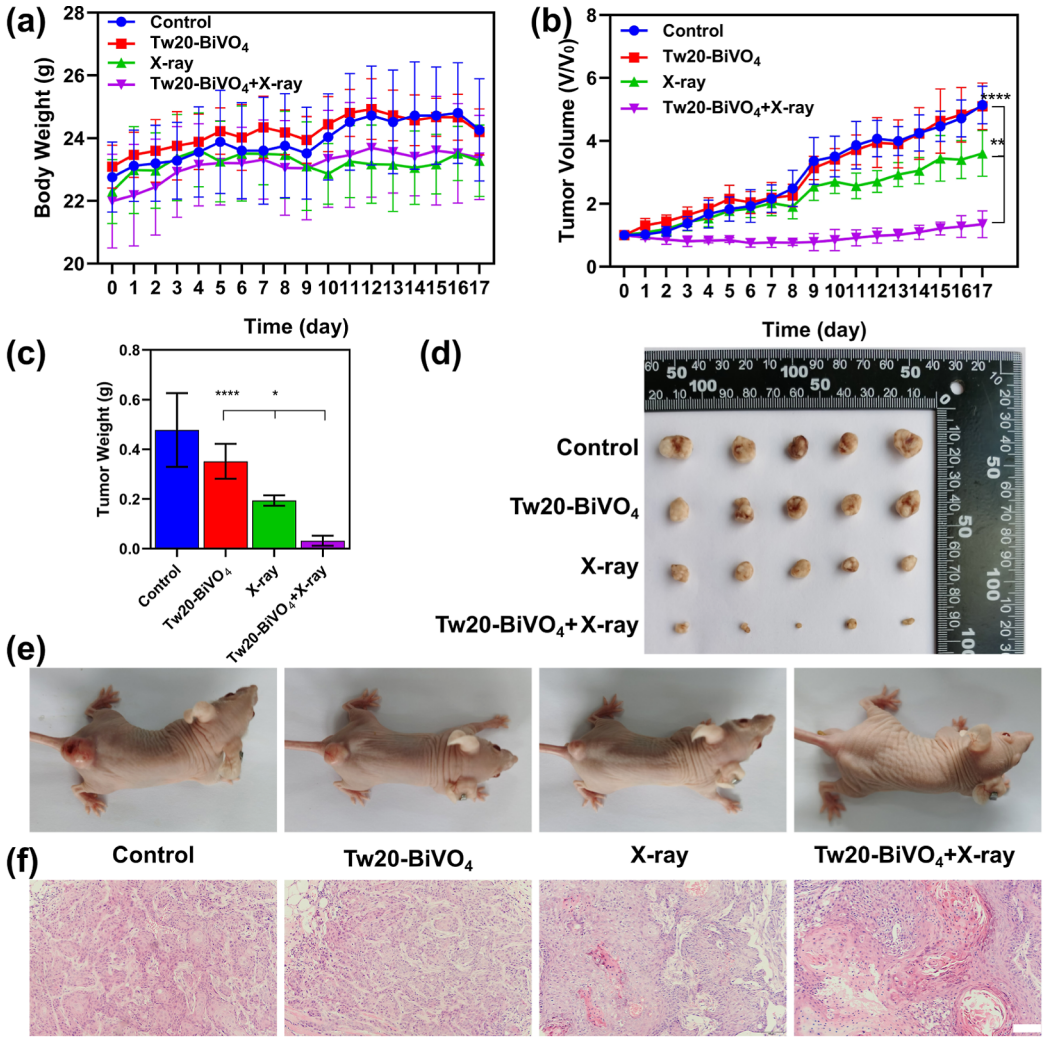

Figure 6. (a) Body weight changes of mice in each group within 17 days after the treatments, determined using ordinary one-way ANOVA. (b) Tumor volume change of mice in each group within 17 days after the treatments, determined using ordinary one-way ANOVA. (c) Final tumor masses of mice in each group after the treatments, determined using ordinary one-way ANOVA. (d) Final tumor photos of mice in each group after the treatments. (e) Final mice photos in each group after the treatments. (f) Hematoxylin and eosin (H&E)-stained tumor tissue slices of mice in each group. The scale bar is 100 μm. *P < 0.05, **P < 0.01, and ****P < 0.0001.

The localization of the tumor and the delineation of the boundary of the tumor by CT imaging are helpful for the application of precise radiotherapy, which not only enhances the efficacy but also reduces the side effects. In vivo treatment experiments in animal models were divided into four groups: (1) the control group, (2) the Tw20-$BiVO_4$ NRs group, (3) the X-ray group, and (4) the Tw20-$BiVO_4$ NRs + X-ray group. In the experiment, the dose of Tw20-$BiVO_4$ NRs was 250 μg (5 mg/mL, 50 μL) and the intensity of the applied X-ray was 6 Gy. Throughout the treatment, the body weights and tumor sizes of the mice were recorded every day to the 17th day. On the 17th day, we took pictures of each tumor-bearing nude mouse and then killed the mice to weigh the tumor and take pictures to compare the weight and size of the tumor in each group.

Changes in the body weight of mice can reflect the state of the body. As shown in Figure 6a, in the control group and the Tw20-$BiVO_4$ NRs group, weight fluctuations were due to tumor growth. In the X-ray group, fluctuating weight loss was due to the minor side effect of the X-rays. However, the body weight of the mice in the Tw20-$BiVO_4$ NRs + X-ray group basically maintained a steady increase, indicating that the mice grew in a good state, which reflects the effect of the treatment (Figure 6a).

In the control group, the tumor growth was not affected and maintained a rapid and stable growth rate (Figure 6b). The average tumor volume increased to 5.1 times of that at the beginning of the experiment, and the average tumor mass was as high as 0.48 g (Figure 6b−e). The average tumor size in the Tw20-$BiVO_4$ NRs group was slightly smaller than that in the control group, and the average tumor mass was also lighter, indicating that Tw20-$BiVO_4$ NRs themselves had a little inhibitory effect on tumor growth (Figure 6b−e). It is worth noting that because of the slight deviation caused by the coverage of the tumor by the mouse skin, the measurement of the long diameter and short diameter of the tumors is based on the naked eye observation, and, a slight deviation is thus inevitable. Therefore, although Figure 6b does not visually show the effect of the Tw20-$BiVO_4$ group, Figure 6c−e does. Tumors in the X-ray group showed a little bit slower growth rate as compared to the control group, revealing the radiotherapy effects of X-ray irradiation (Figure 6b).

https://doi.org/10.1021/acsomega.2c06714
ACS Omega 2023, 8, 4736−4746

Compared with the beginning of the experiment, the tumor size in this group increased about 3.6 times, with an average weight of 0.19 g (Figure 6b,c). The photos of the tumors and the mice visually show the effect of radiotherapy (Figure 6d,e). Radiotherapy inhibited tumor growth to some extent, but we found that the tumor growth rate was still at a high level. Therefore, we further investigated the efficacy of radiotherapy in the presence of a radiosensitizer. In the Tw20-$BiVO_4$ NRs + X-ray group, the tumor growth was severely inhibited, and the tumor size even decreased within the first week after X-ray irradiation (Figure 6b). At the end of the treatment, the average volume of the tumors in this group was 1.3 times of that at the beginning of the experiment, and the average weight was only 0.032 g (Figure 6b,c). Over the course of the treatment, only a small amount of tumor growth occurred and the radiosensitizer greatly enhanced the effect of radiotherapy (Figure 6d,e). Histopathologic staining was also used to evaluate the treatment effect of the tumors in each group. The H&E-stained tumor sections showed the degree of tumor necrosis. In the control group, the tumor basically maintained a normal state, while in the Tw20-$BiVO_4$ NRs + X-ray group, death, nucleus rupture, and ablation of cancer cells can be found, indicating that Tw20-$BiVO_4$ NRs could enhance the treatment effect of radiotherapy (Figure 6f).

At last, H&E-stained slices of major organs were used to prove the biosafety of Tw20-$BiVO_4$ NRs in the treatment in vivo. Compared with the control group, no significant difference in major organs (heart, liver, spleen, lung, kidney, and testis) was observed (Figure 7). Serum biochemistry

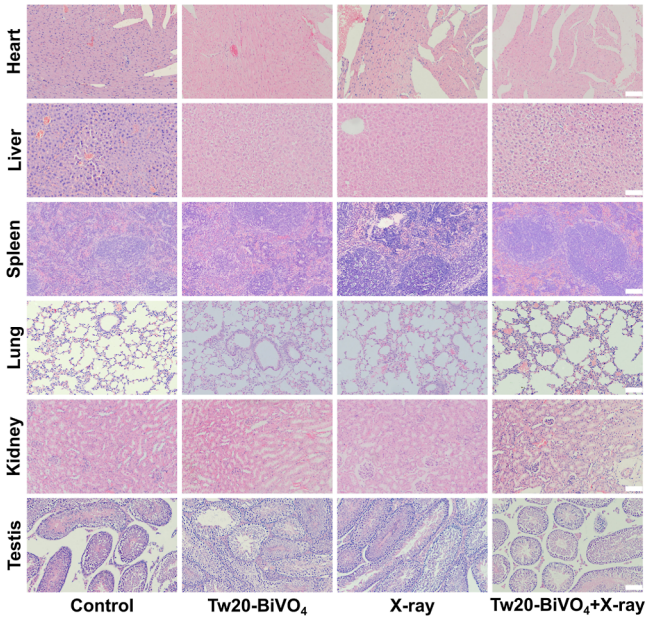

Figure 7. H&E-stained slices of the heart, liver, spleen, lung, kidney, and testis of mice in each group after treatment. The scale bar is 100 μm.

analysis further exhibited the negligible side effects of treatment based on Tw20-$BiVO_4$ NRs. Blood ion, liver function, and renal function tests are shown in Figures S5–S7. All the results above support that Tw20-$BiVO_4$ NRs have preeminent radiosensitizing efficacy and good biocompatibility during the therapeutic process.

CONCLUSIONS

In summary, we succeeded in designing and preparing Tw20-$BiVO_4$ NRs and further used them in the radiotherapy of oral cancer. Because of the high atomic number of Bi, Tw20-$BiVO_4$ NRs are not only a kind of CT imaging contrast agent but also can be used as radiosensitizers. Tw20-$BiVO_4$ NRs can effectively increase intracellular ROS and induce DNA double-strand break damage, leading to the cells' apoptosis. The in vivo experiments prove that our Tw20-$BiVO_4$ NRs with no notable toxicity can identify the location of the tumor on CT imaging. Further combined with X-ray irradiation, the apoptosis of tumor cells can be induced, the growth of the tumor can be inhibited, and the efficacy of radiotherapy can be enhanced. Tw20-$BiVO_4$ NRs have potential application in CT imaging-guided radiotherapy.

EXPERIMENTAL SECTION

Materials. All the chemical reagents used in this work were analytically pure. Tween-20, NH_4VO_3 (99.9%), and $Bi(NO_3)_3{\cdot}5H_2O$ (99.0%) were purchased from Aladdin. Octadecene (ODE, 90%), OLA (>70%), and OA (90%) were purchased from Sigma-Aldrich. The crystal violet staining solution, ROS assay kit, Hoechst 33342, a cell culture medium, and trypsin–ethylenediaminetetraacetic acid were purchased from Beyotime. The annexin V-FITC/PI apoptosis detection kit was purchased from Beijing Solarbio Science & Technology Co. Ltd. The γ-H2AX (phospho-S139) antibody [EP854(2)Y] (Alexa Fluor 568) (ab206901) was purchased from Abcam. Male BALB/c nude mice were purchased from Beijing Vital River Laboratory Animal Technology Co., Ltd. Ultrapure water was used in all of our experiments.

Preparation of $BiVO_4$ NRs. In a three-necked flask, 1 mmol $Bi(NO_3)_3{\cdot}5H_2O$, 10 mL ODE, 2 mL OA, and 2 mL OLA were mixed and heated to 175 °C under nitrogen. When $Bi(NO_3)_3{\cdot}5H_2O$ was completely dissolved, the mixture was cooled to 130 °C, and NH_4VO_3 aqueous solution (0.8 mmol NH_4VO_3 dissolved in 10 mL deionized water) was added rapidly. The mixture was continued to be heated at 100 °C for 30 min and then the heating was stopped to end the reaction. In order to purify the $BiVO_4$ NRs, 10 mL ethanol was added to the mixture and mixed well. Then, the lower aqueous layer was removed, and the upper oil phase was added with 5 mL ethanol and centrifuged at 6000 rpm for 3 min. The precipitate was redispersed in cyclohexane, and this step was repeated twice. The as-prepared $BiVO_4$ NRs were finally dispersed in cyclohexane.

Surface Modification by Tween-20. 40 mg $BiVO_4$ NRs and 200 μL Tween-20 were dissolved in 16 mL cyclohexane, and the mixture was added into 40 mL deionized water under sonication. Then, the cyclohexane was thoroughly evaporated to dryness under stirring. In a 70 °C water bath, the remaining aqueous solution was centrifuged at 8000 rpm for 5 min, and the precipitate was redispersed in deionized water to obtain Tw20-$BiVO_4$ NRs.

In Vitro CT Imaging Assay. In CT imaging assay in vitro, ultrapure water was used to dissolve Tw20-$BiVO_4$ NRs or diatrizoate meglumine solutions into solutions of different concentrations, with concentration gradients of 0, 0.625, 1.25, 2.5, and 5 mg/mL, respectively. A CT machine was used to test the effect of CT imaging. To more intuitively reflect the effect of CT imaging, the corresponding CT signal value of each sample was read in the reading system and the signal

https://doi.org/10.1021/acsomega.2c06714
ACS Omega 2023, 8, 4736–4746

intensity of each group was compared by a numerical value. (The voltage was 60 kV, the current was 1 mA, and the radiation dose was 0.1 mGy.)

In Vitro Cell Viability. Human tongue carcinoma (CAL27) cells, also known as Centre Antoine Lacassagne-27 cells, were developed by J. Gioanni in 1982 and stemmed from a lesion in the middle of the tongue of a 56 year old white male. CAL 27 cells were cultured in Dulbecco's modified Eagle's medium containing 10% (v/v) fetal bovine serum and 1% (v/v) penicillin/streptomycin at 37 °C in a humidified 5% CO_2 incubator. CAL27 cells were separately seeded in a six-well plate (4×10^5 cells/well) and cultured for 24 h. Then, the CAL27 cells were incubated with different concentrations of Tw20-$BiVO_4$ NRs (0, 20, 50, 100, 150, and 200 μg/mL) for another 24 h. The cellular viability was evaluated using the annexin V-FITC/PI apoptosis detection kit and flow cytometry (BD LSRFortessa). In order to ensure the accuracy of the experimental results, we repeated the experiment three times. We also calculated the average and variance of the results of the three experiments to reflect the experimental effect more intuitively.

In Vitro Colony Formation Assay. The clonogenic assay is a well-established in vitro method for assessing radiosensitivity.[55] CAL27 cells were seeded in a six-well plate (2000 cells/well) for 24 h and divided into four groups, namely the control group, the Tw20-$BiVO_4$ NRs group, the X-ray group, and the Tw20-$BiVO_4$ NRs + X-ray group. In the experiment, the concentration of Tw20-$BiVO_4$ NRs cocultured with cells was 100 μg/mL, and the irradiation intensity was 2 Gy. Then, the cells in all groups were washed with phosphate-buffered saline (PBS) three times and cultured with 2 mL of cell culture medium for 10−15 days until the formation of visible colonies. Next, the plates were rinsed three times with PBS and fixed with 4% paraformaldehyde at room temperature for 15 min, followed by rinsing three times with ultrapure water. At last, the cells were stained by a crystal violet staining solution for 10 min, washed with ultrapure water, and photographed by a microscope.

Based on this experiment, we compared the effects of radiotherapy in the presence or absence of Tw20-$BiVO_4$ NRs. After being incubated with or without Tw20-$BiVO_4$ NRs (100 μg/mL) for 24 h, cells were treated by X-rays of different intensities (0, 2, 4, 6, and 8 Gy). Then, the cells were stained with crystal violet as described above, and for the calculation of survival fraction, the formula used was as (surviving colonies)/(cells seeded × plating efficiency).

Apoptosis Assay. CAL27 cells were cultured in six-well plates (1×10^5 cells per well). After complete adherence (48 h), the cells were cultured with or without Tw20-$BiVO_4$ NRs (100 μg/mL) for 24 h. Then, the cells were treated by X-rays (0, 2, 4, 6, and 8 Gy) and sequentially cultured for 24 h after being washed with PBS twice. Annexin V-FITC/PI double staining was used to assess tumor cell apoptosis, and the data were obtained by flow cytometry (BD LSRFortessa).

Detection of Intracellular ROS Generation. DCFH-DA was selected as the fluorescent probe for the study of ROS generation. DCFH-DA can be hydrolyzed to DCFH inside the cell, which is then oxidized by ROS to form a fluorescent compound, 2′,7′-dichlorofluorescein (DCF) (emission wavelength, 525 nm; excitation wavelength, 488 nm).[56,57] CAL27 cells were seeded in confocal dishes (1×10^5 cells/well) for 24 h. Then, the cells were divided into four groups: (1) the control group, (2) the Tw20-$BiVO_4$ NRs group, (3) the X-ray group, and (4) the Tw20-$BiVO_4$ NRs + X-ray group. After the cells in groups (2) and (4) were incubated with Tw20-$BiVO_4$ NRs (100 μg/mL) overnight, cells were washed with PBS three times and incubated with 1.5 mL cell culture medium containing DCFH-DA (1:1000, v/v) and Hoechst 33342 (1:100, v/v) (emission wavelength, 461 nm; excitation wavelength, 350 nm) for 20−40 min. Then, the cells were washed with the cell culture medium three times and cells in groups (3) and (4) were irradiated using X-rays (6 Gy). Finally, the intracellular ROS level was observed by confocal laser scanning microscopy.

In the quantitative analysis of ROS generation, flow cytometry was employed. After performing the same experiment as in the above step, the cells were collected after digestion, washed with PBS, and detected by flow cytometry (BD LSRFortessa).

Detection of Intracellular Chromosome Damage. To evaluate the Tw20-$BiVO_4$ NRs' enhanced chromosome damage induced by X-ray irradiation, CAL27 cells were planted in confocal dishes (1×10^5 cells/well) and incubated for 24 h. The experiments were divided into four groups: (1) the control group, (2) the Tw20-$BiVO_4$ NRs group, (3) the X-ray group, and (4) the Tw20-$BiVO_4$ NRs + X-ray group. Then, the cells in groups (2) and (4) were incubated with Tw20-$BiVO_4$ NRs (100 μg/mL) for 24 h and washed with PBS three times. Then, groups (3) and (4) were irradiated by X-rays (6 Gy). After another 4 h of incubation, cells were fixed by Immunol staining fix solution for 10 min, followed by washing with Immunol staining wash buffer three times. Cells were then permeabilized with immunostaining permeabilization buffer with Triton X-100 for 15 min and washed using Immunol staining wash buffer twice. Next, QuickBlock blocking buffer for Immunol staining was added to the cells for another 1 h at room temperature and further incubated with the γ-H2AX (phospho-S139) antibody [EP854(2)Y] (Alexa Fluor 568) (ab206901) (emission wavelength, 617 nm; excitation wavelength, 590 nm) (1:1000, v/v) at 4 °C overnight. After washing with Immunol staining wash buffer three times, the cell nuclei were stained with Hoechst 33342 (emission wavelength, 461 nm; excitation wavelength, 350 nm) (1:100, v/v) and washed again with Immunol staining wash buffer three times. At last, the intracellular chromosome damage level was observed by confocal laser scanning microscopy.

Animal Experiments. To establish the animal models, the middle of the buttock near the tail of balb/c nude mice were subcutaneously implanted with 200 μL cell suspension containing 1.5×10^6 CAL27 cells. All animal experiments were performed following the Guidelines for the Care and Use of Laboratory Animals from Jilin University and approved by the Animal Ethics Committee of the College of Basic Medical Sciences, Jilin University. Tumor-bearing balb/c nude mice were injected with 50 μL of Tw20-$BiVO_4$ NRs (5 mg/mL) or diatrizoate meglumine solutions through the tail vein to compare the performance of in vivo CT imaging, and Planmeca Cone beam CT (60 kV, 1 mA) was employed for related research.

When the average tumor volume reached 60 mm^3, the mice were randomly divided into four groups on the basis of different treatments: (1) the control group, (2) the Tw20-$BiVO_4$ NRs group, (3) the X-ray group, and (4) the Tw20-$BiVO_4$ NRs + X-ray group. The tumor-bearing mice in groups (1) and (3) were intravenously injected with 50 μL of saline, and the tumor-bearing mice in groups (2) and (4) were

https://doi.org/10.1021/acsomega.2c06714
ACS Omega 2023, 8, 4736−4746

intravenously injected with 50 μL of Tw20-$BiVO_4$ NRs solution (5 mg/mL). After 24 h, the tumors of mice in groups (3) and (4) were exposed to X-rays (6 Gy) using an X-ray biological irradiator. Then, the tumor sizes and body weights of mice in each group were recorded every day after treatments up to the 17th day. The tumor volume was calculated by the formula: $ab^2/2$ (a/b represents the long-/short-axis length of tumors measured by the Vernier caliper, respectively).

Biosafety Studies. At the end of the experiment, serum samples were taken for blood analysis, including ions, liver function, and renal function tests. Then, all the mice were euthanized, and the major organs (including the heart, liver, spleen, lung, kidney, and testis) and tumors were dissected, fixed with 4% paraformaldehyde, and used for H&E staining. H&E-stained sections were photographed using an optical microscope.

Statistical Analysis. The collected experimental data were analyzed using Student's t test or one-way analysis of variance. The results were presented as mean ± standard deviation of three independent experiments. P values less than 0.05 were considered to be significant.

■ ASSOCIATED CONTENT

Supporting Information

The Supporting Information is available free of charge at https://pubs.acs.org/doi/10.1021/acsomega.2c06714.

Additional cell apoptosis determined by flow cytometry, intracellular ROS level determined by flow cytometry, ion tests, liver function tests, and renal function tests (PDF)

■ AUTHOR INFORMATION

Corresponding Author

Zhimin Li − *Department of Oral Radiology, School of Stomatology, China Medical University, Shenyang 110002, P. R. China*; orcid.org/0000-0003-0892-4999; Email: zmli@cmu.edu.cn

Authors

Bo Peng − *Department of Oral Radiology, School of Stomatology, China Medical University, Shenyang 110002, P. R. China*

Yifan Hao − *Department of Oral Radiology, Hospital of Stomatology, Jilin University, Changchun 130021, P. R. China*

Chao Si − *Department of Oral Radiology, Hospital of Stomatology, Jilin University, Changchun 130021, P. R. China*

Bo Wang − *Department of Oral Radiology, School of Stomatology, China Medical University, Shenyang 110002, P. R. China*

Chengfeng Luo − *Department of Oral Radiology, School of Stomatology, China Medical University, Shenyang 110002, P. R. China*

Menghao Chen − *Department of Oral Radiology, School of Stomatology, China Medical University, Shenyang 110002, P. R. China*

Cheng Luo − *Department of Orthodontics, School of Stomatology, China Medical University, Shenyang 110002, P. R. China*

Baijuan Gong − *Department of Orthodontics, School of Stomatology, China Medical University, Shenyang 110002, P. R. China*

Complete contact information is available at: https://pubs.acs.org/10.1021/acsomega.2c06714

Author Contributions

Z.M.L. supervised and proposed the project. B.P. and Y.F.H. designed and performed the experiments. B.P., Y.F.H., B.J.G., and Z.M.L. co-wrote the paper. C.S., B.W., C.F.L., M.H.C., and C.L. participated in most experiments. All authors have given their approval for the final version of the manuscript.

Notes

The authors declare no competing financial interest.

■ ACKNOWLEDGMENTS

This work was supported by the Medical Engineering Intersection Joint Funds of the Natural Science Foundation of Liaoning Province of China (2021-YGJC-18) and the Science and Technology Project of Jilin Provincial Department of Education (JJKH20201109KJ).

■ REFERENCES

(1) Shield, K. D.; Ferlay, J.; Jemal, A.; Sankaranarayanan, R.; Chaturvedi, A. K.; Bray, F.; Soerjomataram, I. The global incidence of lip, oral cavity, and pharyngeal cancers by subsite in 2012. *Ca-Cancer J. Clin.* **2017**, *67*, 51−64.

(2) Torre, L. A.; Bray, F.; Siegel, R. L.; Ferlay, J.; Lortet-Tieulent, J.; Jemal, A. Global cancer statistics, 2012. *Ca-Cancer J. Clin.* **2015**, *65*, 87−108.

(3) Bray, F.; Ferlay, J.; Soerjomataram, I.; Siegel, R. L.; Torre, L. A.; Jemal, A. Global cancer statistics 2018: GLOBOCAN estimates of incidence and mortality worldwide for 36 cancers in 185 countries. *Ca-Cancer J. Clin.* **2018**, *68*, 394−424.

(4) Chi, A. C.; Day, T. A.; Neville, B. W. Oral cavity and oropharyngeal squamous cell carcinoma-an update. *Ca-Cancer J. Clin.* **2015**, *65*, 401−421.

(5) Kosugi, A.; Kasahara, M.; Yang, L.; Nakamura-Takahashi, A.; Shibahara, T.; Mori, T. Method for diagnosing neoplastic lesions by quantitative fluorescence value. *Sci. Rep.* **2019**, *9*, 7833.

(6) Civantos, F. J.; Zitsch, R. P.; Schuller, D. E.; Agrawal, A.; Smith, R. B.; Nason, R.; Petruzelli, G.; Gourin, C. G.; Wong, R. J.; Ferris, R. L.; El Naggar, A.; Ridge, J. A.; Paniello, R. C.; Owzar, K.; McCall, L.; Chepeha, D. B.; Yarbrough, W. G.; Myers, J. N. Sentinel lymph node biopsy accurately stages the regional lymph nodes for T_1-T_2 oral squamous cell carcinomas: results of a prospective multi-institutional trial. *J. Clin. Oncol.* **2010**, *28*, 1395−1400.

(7) Schaue, D.; McBride, W. H. Opportunities and challenges of radiotherapy for treating cancer. *Nat. Rev. Clin. Oncol.* **2015**, *12*, 527−540.

(8) Caudell, J. J.; Torres-Roca, J. F.; Gillies, R. J.; Enderling, H.; Kim, S.; Rishi, A.; Moros, E. G.; Harrison, L. B. The future of personalised radiotherapy for head and neck cancer. *Lancet Oncol.* **2017**, *18*, e266−e273.

(9) Wang, H.; Mu, X.; He, H.; Zhang, X. D. Cancer Radiosensitizers. *Trends Pharmacol. Sci.* **2018**, *39*, 24−48.

(10) De Ruysscher, D.; Niedermann, G.; Burnet, N. G.; Siva, S.; Lee, A. W. M.; Hegi-Johnson, F. Radiotherapy toxicity. *Nat. Rev. Dis. Prim.* **2019**, *5*, 13.

(11) Tang, L.; Wei, F.; Wu, Y.; He, Y.; Shi, L.; Xiong, F.; Gong, Z.; Guo, C.; Li, X.; Deng, H.; Cao, K.; Zhou, M.; Xiang, B.; Li, X.; Li, Y.; Li, G.; Xiong, W.; Zeng, Z. Role of metabolism in cancer cell radioresistance and radiosensitization methods. *J. Exp. Clin. Cancer Res.* **2018**, *37*, 87.

(12) Srinivas, U. S.; Tan, B. W. Q.; Vellayappan, B. A.; Jeyasekharan, A. D. ROS and the DNA damage response in cancer. *Redox Biol.* **2019**, *25*, 101084.
(13) Lee, S. Y.; Jeong, E. K.; Ju, M. K.; Jeon, H. M.; Kim, M. Y.; Kim, C. H.; Park, H. G.; Han, S. I.; Kang, H. S. Induction of metastasis, cancer stem cell phenotype, and oncogenic metabolism in cancer cells by ionizing radiation. *Mol. Cancer* **2017**, *16*, 10.
(14) Goel, S.; Ni, D.; Cai, W. Harnessing the Power of Nanotechnology for Enhanced Radiation Therapy. *ACS Nano* **2017**, *11*, 5233−5237.
(15) Xie, J.; Gong, L.; Zhu, S.; Yong, Y.; Gu, Z.; Zhao, Y. Emerging Strategies of Nanomaterial-Mediated Tumor Radiosensitization. *Adv. Mater.* **2019**, *31*, 1802244.
(16) Kunz-Schughart, L. A.; Dubrovska, A.; Peitzsch, C.; Ewe, A.; Aigner, A.; Schellenburg, S.; Muders, M. H.; Hampel, S.; Cirillo, G.; Iemma, F.; Tietze, R.; Alexiou, C.; Stephan, H.; Zarschler, K.; Vittorio, O.; Kavallaris, M.; Parak, W. J.; Mädler, L.; Pokhrel, S. Nanoparticles for radiooncology: Mission, vision, challenges. *Biomaterials* **2017**, *120*, 155−184.
(17) Retif, P.; Pinel, S.; Toussaint, M.; Frochot, C.; Chouikrat, R.; Bastogne, T.; Barberi-Heyob, M. Nanoparticles for Radiation Therapy Enhancement: the Key Parameters. *Theranostics* **2015**, *5*, 1030−1044.
(18) Song, G.; Cheng, L.; Chao, Y.; Yang, K.; Liu, Z. Emerging Nanotechnology and Advanced Materials for Cancer Radiation Therapy. *Adv. Mater.* **2017**, *29*, 1700996.
(19) Zhang, C.; Yan, L.; Gu, Z.; Zhao, Y. Strategies based on metal-based nanoparticles for hypoxic-tumor radiotherapy. *Chem. Sci.* **2019**, *10*, 6932−6943.
(20) Liu, Y.; Zhang, P.; Li, F.; Jin, X.; Li, J.; Chen, W.; Li, Q. Metal-based NanoEnhancers for Future Radiotherapy: Radiosensitizing and Synergistic Effects on Tumor Cells. *Theranostics* **2018**, *8*, 1824−1849.
(21) Lusic, H.; Grinstaff, M. W. X-ray-computed tomography contrast agents. *Chem. Rev.* **2013**, *113*, 1641−1666.
(22) Hernández-Rivera, M.; Kumar, I.; Cho, S. Y.; Cheong, B. Y.; Pulikkathara, M. X.; Moghaddam, S. E.; Whitmire, K. H.; Wilson, L. J. High-Performance Hybrid Bismuth-Carbon Nanotube Based Contrast Agent for X-ray CT Imaging. *ACS Appl. Mater. Interfaces* **2017**, *9*, 5709−5716.
(23) Huang, W.; He, L.; Zhang, Z.; Shi, S.; Chen, T. Shape-Controllable Tellurium-Driven Heterostructures with Activated Robust Immunomodulatory Potential for Highly Efficient Radiophotothermal Therapy of Colon Cancer. *ACS Nano* **2021**, *15*, 20225−20241.
(24) Dong, X.; Cheng, R.; Zhu, S.; Liu, H.; Zhou, R.; Zhang, C.; Chen, K.; Mei, L.; Wang, C.; Su, C.; Liu, X.; Gu, Z.; Zhao, Y. A Heterojunction Structured $WO_{2.9}$-WSe_2 Nanoradiosensitizer Increases Local Tumor Ablation and Checkpoint Blockade Immunotherapy upon Low Radiation Dose. *ACS Nano* **2020**, *14*, 5400−5416.
(25) Liu, J.; Zhang, J.; Huang, F.; Deng, Y.; Li, B.; Ouyang, R.; Miao, Y.; Sun, Y.; Li, Y. X-ray and NIR light dual-triggered mesoporous upconversion nanophosphor/Bi heterojunction radiosensitizer for highly efficient tumor ablation. *Acta Biomater.* **2020**, *113*, 570−583.
(26) Du, J.; Gu, Z.; Yan, L.; Yong, Y.; Yi, X.; Zhang, X.; Liu, J.; Wu, R.; Ge, C.; Chen, C.; Zhao, Y. Poly(Vinylpyrollidone)- and Selenocysteine-Modified Bi_2Se_3 Nanoparticles Enhance Radiotherapy Efficacy in Tumors and Promote Radioprotection in Normal Tissues. *Adv. Mater.* **2017**, *29*, 1701268.
(27) Wang, X.; Zhang, C.; Du, J.; Dong, X.; Jian, S.; Yan, L.; Gu, Z.; Zhao, Y. Enhanced Generation of Non-Oxygen Dependent Free Radicals by Schottky-type Heterostructures of Au-Bi_2S_3 Nanoparticles via X-ray-Induced Catalytic Reaction for Radiosensitization. *ACS Nano* **2019**, *13*, 5947−5958.
(28) Zang, Y.; Gong, L.; Mei, L.; Gu, Z.; Wang, Q. Bi_2WO_6 Semiconductor Nanoplates for Tumor Radiosensitization through High-Z Effects and Radiocatalysis. *ACS Appl. Mater. Interfaces* **2019**, *11*, 18942−18952.
(29) Liu, J.; Zhang, Y.; Li, Q.; Feng, Z.; Huang, P.; Wang, W.; Liu, J. Development of injectable thermosensitive polypeptide hydrogel as facile radioisotope and radiosensitizer hotspot for synergistic brachytherapy. *Acta Biomater.* **2020**, *114*, 133−145.
(30) Yan, J.; Wang, G.; Xie, L.; Tian, H.; Li, J.; Li, B.; Sang, W.; Li, W.; Zhang, Z.; Dai, Y. Engineering Radiosensitizer-Based Metal-Phenolic Networks Potentiate STING Pathway Activation for Advanced Radiotherapy. *Adv. Mater.* **2022**, *34*, 2105783.
(31) Fan, W.; Tang, W.; Lau, J.; Shen, Z.; Xie, J.; Shi, J.; Chen, X. Breaking the Depth Dependence by Nanotechnology-Enhanced X-Ray-Excited Deep Cancer Theranostics. *Adv. Mater.* **2019**, *31*, 1806381.
(32) Cheng, Y.; Zhang, H. Novel Bismuth-Based Nanomaterials Used for Cancer Diagnosis and Therapy. *Chemistry* **2018**, *24*, 17405−17418.
(33) Wang, Z.; Liu, S.; Wang, L.; Zou, H.; Wang, Z.; Tang, X.; Feng, W.; Chong, Y.; Liu, Y.; Yang, B.; Zhang, H. $BiVO_4$@Bi_2S_3 Heterojunction Nanorods with Enhanced Charge Separation Efficiency for Multimodal Imaging and Synergy Therapy of Tumor. *ACS Appl. Bio Mater.* **2020**, *3*, 5080−5092.
(34) Hu, X.; Sun, J.; Li, F.; Li, R.; Wu, J.; He, J.; Wang, N.; Liu, J.; Wang, S.; Zhou, F.; Sun, X.; Kim, D.; Hyeon, T.; Ling, D. Renal-Clearable Hollow Bismuth Subcarbonate Nanotubes for Tumor Targeted Computed Tomography Imaging and Chemoradiotherapy. *Nano Lett.* **2018**, *18*, 1196−1204.
(35) Badrigilan, S.; Choupani, J.; Khanbabaei, H.; Hoseini-Ghahfarokhi, M.; Webster, T. J.; Tayebi, L. Bismuth-Based Nanomaterials: Recent Advances in Tumor Targeting and Synergistic Cancer Therapy Techniques. *Adv. Healthcare Mater.* **2020**, *9*, 1901695.
(36) Liu, J.; Zheng, X.; Yan, L.; Zhou, L.; Tian, G.; Yin, W.; Wang, L.; Liu, Y.; Hu, Z.; Gu, Z.; Chen, C.; Zhao, Y. Bismuth sulfide nanorods as a precision nanomedicine for in vivo multimodal imaging-guided photothermal therapy of tumor. *ACS Nano* **2015**, *9*, 696−707.
(37) Jakhmola, A.; Anton, N.; Vandamme, T. F. Inorganic nanoparticles based contrast agents for X-ray computed tomography. *Adv. Healthcare Mater.* **2012**, *1*, 413−431.
(38) Badrigilan, S.; Heydarpanahi, F.; Choupani, J.; Jaymand, M.; Samadian, H.; Hoseini-Ghahfarokhi, M.; Webster, T. J.; Tayebi, L. A Review on the Biodistribution, Pharmacokinetics and Toxicity of Bismuth-Based Nanomaterials. *Int. J. Nanomed.* **2020**, *15*, 7079−7096.
(39) Liu, Y.; Ai, K.; Lu, L. Nanoparticulate X-ray computed tomography contrast agents: from design validation to in vivo applications. *Acc. Chem. Res.* **2012**, *45*, 1817−1827.
(40) Ashton, J. R.; West, J. L.; Badea, C. T. In vivo small animal micro-CT using nanoparticle contrast agents. *Front. Pharmacol.* **2015**, *6*, 256.
(41) Hsu, J. C.; Nieves, L. M.; Betzer, O.; Sadan, T.; Noël, P. B.; Popovtzer, R.; Cormode, D. P. Nanoparticle contrast agents for X-ray imaging applications. *Wiley Interdiscip. Rev.: Nanomed. Nanobiotechnol.* **2020**, *12*, 1642.
(42) Meng, X.; Wu, Y.; Bu, W. Functional CT Contrast Nanoagents for the Tumor Microenvironment. *Adv. Healthcare Mater.* **2021**, *10*, 2000912.
(43) Han, X.; Xu, K.; Taratula, O.; Farsad, K. Applications of nanoparticles in biomedical imaging. *Nanoscale* **2019**, *11*, 799−819.
(44) Zheng, L.; Zhu, R.; Chen, L.; Fu, Q.; Li, J.; Chen, C.; Song, J.; Yang, H. X-ray sensitive high-Z metal nanocrystals for cancer imaging and therapy. *Nano Res.* **2021**, *14*, 3744−3755.
(45) Rabin, O.; Manuel Perez, J.; Grimm, J.; Wojtkiewicz, G.; Weissleder, R. An X-ray computed tomography imaging agent based on long-circulating bismuth sulphide nanoparticles. *Nat. Mater.* **2006**, *5*, 118−122.
(46) Cheng, Y.; Chang, Y.; Feng, Y.; Jian, H.; Wu, X.; Zheng, R.; Xu, K.; Zhang, H. Bismuth Sulfide Nanorods with Retractable Zinc Protoporphyrin Molecules for Suppressing Innate Antioxidant Defense System and Strengthening Phototherapeutic Effects. *Adv. Mater.* **2019**, *31*, 1806808.
(47) Shahbazi, M. A.; Faghfouri, L.; Ferreira, M. P. A.; Figueiredo, P.; Maleki, H.; Sefat, F.; Hirvonen, J.; Santos, H. A. The versatile biomedical applications of bismuth-based nanoparticles and compo-

https://doi.org/10.1021/acsomega.2c06714
ACS Omega 2023, 8, 4736−4746

sites: therapeutic, diagnostic, biosensing, and regenerative properties. *Chem. Soc. Rev.* **2020**, *49*, 1253−1321.
(48) Ding, M.; Liu, J.; Yang, J.; Wang, H.; Xie, X.; Yang, X.; Li, Y.; Guo, N.; Ouyang, R.; Miao, Y. How Do Bismuth-Based Nanomaterials Function as Promising Theranostic Agents for the Tumor Diagnosis and Therapy? *Curr. Med. Chem.* **2022**, *29*, 1866−1890.
(49) Fang, J.; Islam, W.; Maeda, H. Exploiting the dynamics of the EPR effect and strategies to improve the therapeutic effects of nanomedicines by using EPR effect enhancers. *Adv. Drug Delivery Rev.* **2020**, *157*, 142−160.
(50) Golombek, S. K.; May, J. N.; Theek, B.; Appold, L.; Drude, N.; Kiessling, F.; Lammers, T. Tumor targeting via EPR: Strategies to enhance patient responses. *Adv. Drug Delivery Rev.* **2018**, *130*, 17−38.
(51) Tee, J. K.; Yip, L. X.; Tan, E. S.; Santitewagun, S.; Prasath, A.; Ke, P. C.; Ho, H. K.; Leong, D. T. Nanoparticles' interactions with vasculature in diseases. *Chem. Soc. Rev.* **2019**, *48*, 5381−5407.
(52) Ng, T. S. C.; Garlin, M. A.; Weissleder, R.; Miller, M. A. Improving nanotherapy delivery and action through image-guided systems pharmacology. *Theranostics* **2020**, *10*, 968−997.
(53) Wang, Z.; Wang, G.; Kang, T.; Liu, S.; Wang, L.; Zou, H.; Chong, Y.; Liu, Y. $BiVO_4/Fe_3O_4$@polydopamine superparticles for tumor multimodal imaging and synergistic therapy. *J. Nanobiotechnol.* **2021**, *19*, 90.
(54) Zhu, Y.; Li, W.; Zhang, Y.; Li, J.; Liang, L.; Zhang, X.; Chen, N.; Sun, Y.; Chen, W.; Tai, R.; Fan, C.; Huang, Q. Excessive sodium ions delivered into cells by nanodiamonds: implications for tumor therapy. *Small* **2012**, *8*, 1771−1779.
(55) Mirzayans, R.; Murray, D. Intratumor Heterogeneity and Therapy Resistance: Contributions of Dormancy, Apoptosis Reversal (Anastasis) and Cell Fusion to Disease Recurrence. *Int. J. Mol. Sci.* **2020**, *21*, 1308.
(56) Dikalov, S. I.; Harrison, D. G. Methods for detection of mitochondrial and cellular reactive oxygen species. *Antioxid. Redox Signaling* **2014**, *20*, 372−382.
(57) Cheng, G.; Zielonka, M.; Dranka, B.; Kumar, S. N.; Myers, C. R.; Bennett, B.; Garces, A. M.; Dias Duarte Machado, L. G.; Thiebaut, D.; Ouari, O.; Hardy, M.; Zielonka, J.; Kalyanaraman, B. Detection of mitochondria-generated reactive oxygen species in cells using multiple probes and methods: Potentials, pitfalls, and the future. *J. Biol. Chem.* **2018**, *293*, 10363−10380.

https://doi.org/10.1021/acsomega.2c06714
ACS Omega 2023, 8, 4736−4746